

Large-Area Fabrication of High-Performance Flexible and Wearable Pressure Sensors

Xiaodong Wu, Yasser Khan, Jonathan Ting, Juan Zhu, Seiya Ono, Xinxing Zhang, Shixuan Du, James W. Evans, Canhui Lu,* and Ana C. Arias*

Flexible pressure sensors with high sensitivity, broad working range, and good scalability are highly desired for the next generation of wearable electronic devices. However, manufacturing of such pressure sensors still remains challenging. A large-area compliant and cost-effective process to fabricate high-performance pressure sensors via a combination of mesh-molded periodic microstructures and printed side-by-side electrodes is presented. The sensors exhibit low operating voltage (1 V), high sensitivity (20.9 kPa^{-1}), low detection limit (7.4 Pa), fast response/recovery time (23/18 ms), and excellent reliability (over 10 000 cycles). More importantly, they exhibit ultra-broad working range (7.4–1 000 000 Pa), high tunability, large-scale production feasibility, and significant advantage in format miniaturization and creating sensor arrays with self-defined patterns. The versatility of these devices is demonstrated in various human activity monitoring and spatial pressure mapping as electronic skins. Furthermore, utilizing printing methods, a flexible smart insole with a high level of integration for both foot pressure and temperature mapping is demonstrated. The scalable and cost-effective manufacturing along with the good comprehensive performance of the pressure sensors makes them very attractive for future development of wearable smart devices and human–machine interfaces.

1. Introduction

Wearable human-interactive devices can improve our quality of life and health. Flexible pressure sensors, as an important element of human-interactive devices, are of great interest and have a wide range of applications such as continuous health monitoring, personal diagnostics, robotics, prostheses, and the Internet of Things. Over the past decade, significant advancement has been achieved in fabricating pressure sensors based on resistive, capacitive, transistive, piezoelectric, and triboelectric sensing mechanisms. For a pressure sensor, two components are necessary: pressure-sensing layers and conductive electrodes. Variation in electrical properties of the sensing layers under applied pressure is collected and transmitted through the conductive electrodes, thus to transduce external mechanical stimuli into electrical signals.

Introducing microstructures into the pressure-sensing layers is an effective way to achieve enhanced performance in detection limit, sensitivity, response/recovery time, and reproducibility.^[1–3] Numerous efforts have been made in recent years to construct pressure-sensing microstructures. One of the most investigated strategies is the use of patterned silicon molds to fabricate uniform and periodic microstructures, including micropyramids,^[4–7] microdomes,^[3,8,9] microgrooves,^[10,11] micropillars,^[12] and microcubes.^[13] Silicon molds are usually on wafer-scale and their preparation is complicated, expensive, and time-consuming, involving traditional lithography and multistep etching processes.^[1,2,14] These drawbacks limit their large-area application despite the effectiveness. Alternative methods for microstructure fabrication have been explored. Silk textile was used as a mold to construct pressure sensitive microstructures, with the working range limited to 1.2 kPa.^[1] Plant leaves^[2,14,15] and abrasive papers^[16,17] were also employed as templates to prepare pressure-sensing microstructures. The size and shape of the microstructures on these templates are randomly distributed with poor uniformity, periodicity, and controllability, which make it challenging to fabricate reproducible pressure sensors from batch to batch. Therefore, the significant trade-off among scalability, fabrication cost, and microstructure quality (i.e., regularity, periodicity,


X. Wu, Y. Khan,^[†] J. Ting, J. Zhu, S. Ono, Prof. A. C. Arias
Department of Electrical Engineering and Computer Sciences
University of California
Berkeley, CA 94720, USA
E-mail: acarias@eecs.berkeley.edu

X. Wu, X. Zhang, Prof. C. Lu
State Key Laboratory of Polymer Materials Engineering
Polymer Research Institute of Sichuan University
Chengdu 610065, China
E-mail: canhuilu@scu.edu.cn

Prof. J. W. Evans
Department of Materials Science and Engineering
University of California
Berkeley, CA 94720, USA

J. Zhu, Prof. S. Du
Institute of Physics & University of Chinese Academy of Sciences
Chinese Academy of Sciences
Beijing 100190, China

^[†]Present address: Department of Chemical Engineering, Stanford University, 443 Via Ortega, Stanford, CA 94305-4125, USA

 The ORCID identification number(s) for the author(s) of this article can be found under <https://doi.org/10.1002/aelm.201901310>.

DOI: 10.1002/aelm.201901310

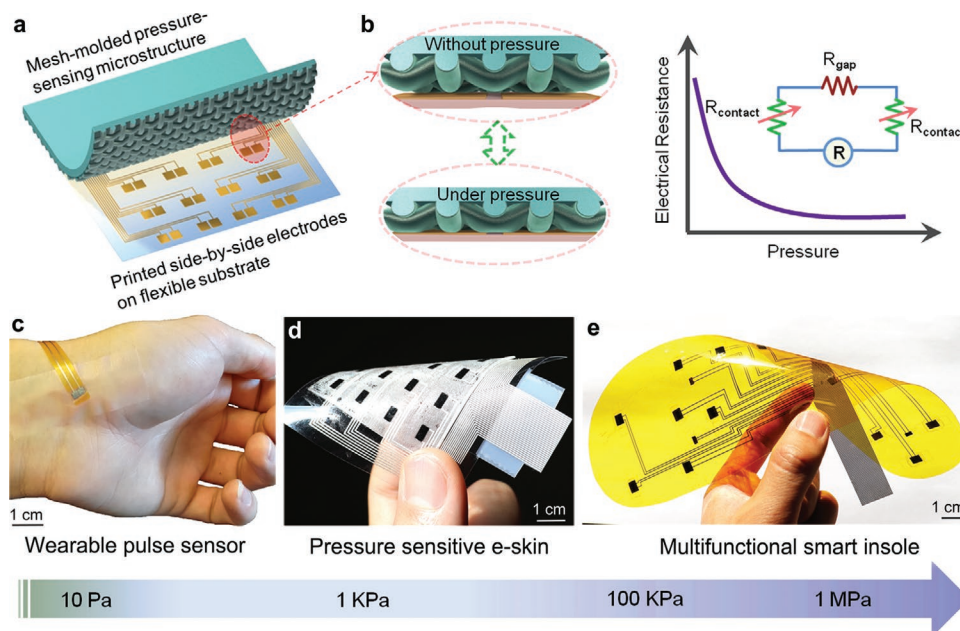


Figure 1. Large-area compliant and high-performance pressure sensors with a broad application range. Schematics showing the layout (a) and operating principle (b) of pressure sensors composed of scalable pressure-sensing microstructures and printed side-by-side electrodes with self-defined patterns. c–e) Photographs showing the broad application range of the pressure sensors, ranging from wearable pulse sensor, flexible pressure sensitive e-skin to a smart insole for simultaneous monitoring of foot pressure and temperature.

and tunability) still remains a big challenge for cost-effective manufacturing of pressure sensors with desirable comprehensive performance. Screen meshes are widely used for separating particles of different sizes. The micro-patterns of screen meshes are very uniform, periodic, and highly tunable in size and periodicity (Figure S1, Supporting Information). Therefore, screen meshes could be ideal molds to construct large-area periodic microstructures. In this work, we realize the scalable fabrication of high-quality pressure-sensing microstructures via a mesh-molding strategy.

In addition to the sensing layer, the electrode configuration of pressure sensors has a big impact on their performance. Top-bottom electrode configurations are the mostly reported sensor layouts with three common scenarios: 1) the pressure-sensing layer is sandwiched between two electrodes;^[18–23] 2) a conductive pressure-sensing microstructure used as an electrode is paired with a flat counter electrode;^[4,24,25] and 3) two conductive microstructures are interlocked with each other.^[1,8,9,12,16] These out-of-plane electrode configurations are suitable to fabricate single pressure sensor but could be disadvantageous for constructing highly integrated devices that require planar interfaces or low profiles. Recently, interdigitated electrodes are used to fabricate flexible pressure sensors.^[26–30] Nevertheless, it is difficult to use the interdigitated electrodes to fabricate sensor arrays with high pixel density. Additionally, these interdigitated electrodes are usually prepared via metal deposition techniques with the assistance of shadow masks, which is time-consuming and not suitable for large-area production. In this study, we propose a novel side-by-side in-plane electrode configuration for fabricating flexible pressure sensors with high sensitivity and ultra-broad working range. Printing techniques are employed to produce the side-by-side electrodes, which can greatly simplify

the conventional fabrication processes and enable high-throughput production of flexible electrodes. More importantly, utilizing printed side-by-side electrodes enables the fabrication of pressure sensor arrays with well-defined patterns, facilitating high-level integration of multifunctional devices.

In our design, we combine the mesh-molded pressure-sensing microstructures with the printed side-by-side electrodes to fabricate large-area compliant and high-performance pressure sensors. The flexible pressure sensors reported here exhibit high sensitivity (20.9 kPa^{-1}), low detection limit (7.4 Pa), ultra-broad working range ($7.4\text{--}1000000 \text{ Pa}$), fast response/recovery ($23/18 \text{ ms}$), good reliability (over 10000 cycles), excellent tunability, and great advantage in format miniaturization ($4 \text{ mm} \times 2 \text{ mm}$) and creating sensor arrays with self-defined patterns. The good performance of our pressure sensors provides a solid platform for monitoring a wide range of human activities as well as resolving spatial distribution and magnitude of external pressure as an electronic skin (e-skin). Moreover, we demonstrate a smart insole with a high level of integration for both foot pressure and temperature mapping, which is promising for foot ulcer prevention/detection, medical diagnostics, and sports applications.

2. Results and Discussion

2.1. Design Concept of the Pressure Sensors

The design concept of our pressure sensors is illustrated in Figure 1a. Briefly, the pressure sensors consist of two components: 1) periodic pressure-sensing microstructures fabricated via a scalable mesh-molding method and 2) printed

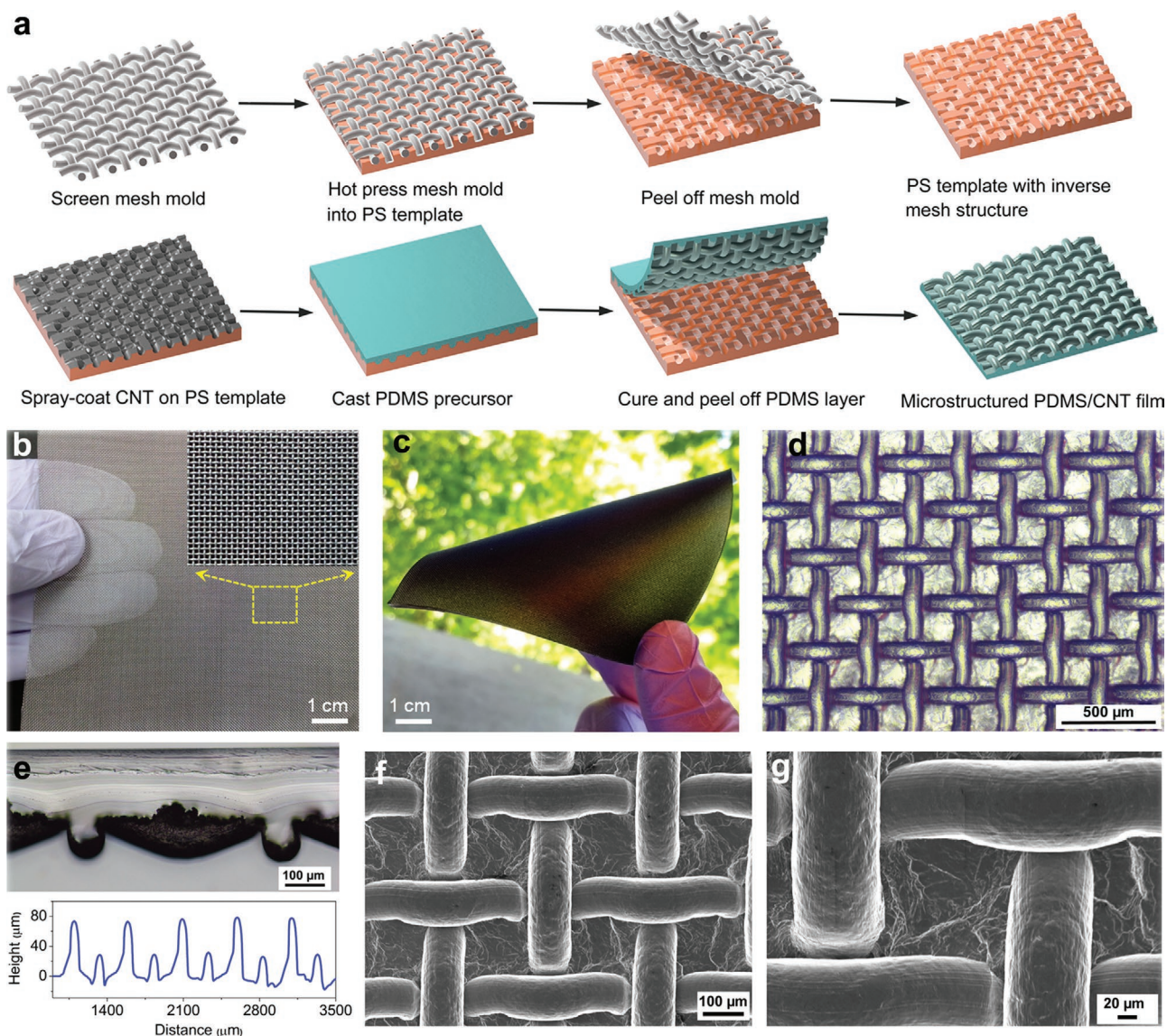


Figure 2. Scalable fabrication of periodic microstructures via mesh-molding strategy. a) Schematic diagram showing the fabrication process flow of the periodic pressure-sensing microstructures. b) Photographs of the stainless-steel screen mesh, which was used as the mold. Insert picture shows the magnified morphology of the uniform and periodic mesh structure. c) Picture of the as-prepared conductive PDMS/CNT microstructured film. d) Optical micrograph of PDMS microstructure molded from the screen mesh. Scale bar: 500 μm . e) Optical image of a sliced PDMS/CNT microstructure and surface profile of the PDMS/CNT microstructure. Scale bar: 100 μm . f, g) SEM images of PDMS/CNT microstructure with different magnifications. Scale bar: 100 μm (f) and 20 μm (g). These optical and SEM images are based on microstructures from a mold of 100 mesh count.

side-by-side electrodes. Unlike most of the reported pressure sensors with top–bottom electrodes,^[1,4,8,9,12,16,18–25] here, we propose a printable side-by-side electrode configuration (Figure 1b), which makes it easy to miniaturize the sensor format (4 mm \times 2 mm, Figure 1c) and also easy to create sensor arrays with self-defined patterns. Moreover, the side-by-side electrode configuration shows higher sensitivity and broader working range when compared to conventional top–bottom electrodes, as discussed below. The operating principle of the pressure sensors is based on pressure regulated variation in contact resistance between the conductive microstructure and each of the two electrodes (Figure 1b, discussed in Section S1, Supporting Information). Combination of the mesh-molded

microstructures and the printed side-by-side electrodes allows us to manufacture pressure sensors with high sensitivity and ultra-broad working range (7.4–1 000 000 Pa), exhibiting good potential of fabricating versatile human–machine interfaces, as presented in Figure 1c–e.

2.2. Scalable Fabrication: Mesh-Molded Microstructures and Printed Electrodes

Figure 2a shows the fabrication procedure of the pressure-sensing microstructures via a mesh-molding strategy. A piece of pre-cleaned screen mesh (Figure 2b) was hot-pressed into

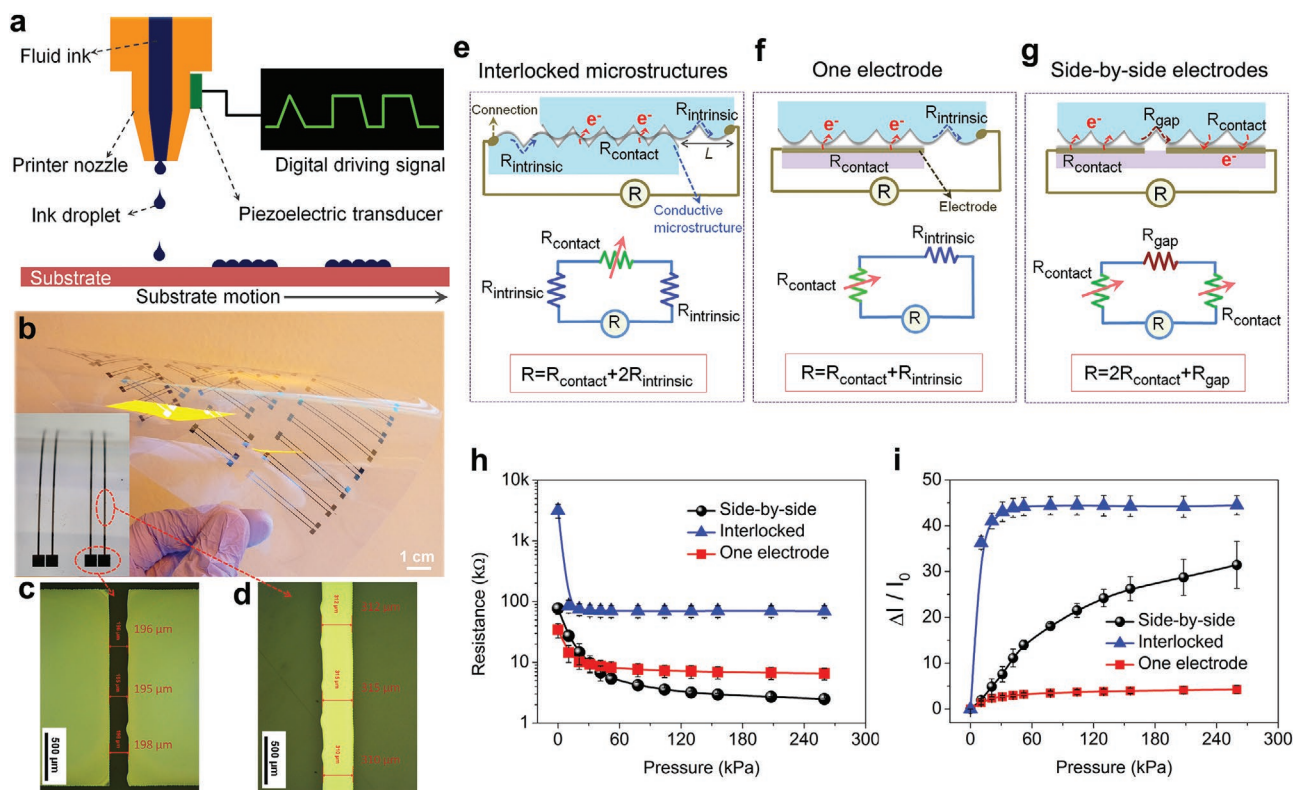


Figure 3. Printed side-by-side electrodes with high sensitivity and broad working range. a) Schematic illustration showing the working principle of inkjet printing. b) Photograph of the inkjet printed flexible electrodes with the side-by-side configuration. c, d) Optical images of the side-by-side electrodes (2 mm × 2 mm) with 200 μm gap and trace lines with 300 μm width. Scale bar: 500 μm for (c) and (d). Schematic illustrations showing the resistance models of pressure sensors with different electrode configurations: interlocked microstructures (e), one electrode configuration (f), and side-by-side electrodes (g). h, i) Comparison in response behaviors of resistance pressure sensors with these three electrode configurations, respectively.

the surface of a polystyrene (PS) sheet. After cooling down, the screen mesh was peeled off from the PS sheet, leaving an inverse mesh microstructure on the PS template (Figure S2, Supporting Information). Then, a conductive carbon nanotube (CNT) layer was uniformly spray-coated on the inverse microstructured PS template, followed by casting a polydimethylsiloxane (PDMS) precursor layer. After curing the PDMS, the conductive and microstructured PDMS/CNT film (Figure 2c) was peeled off, with a robust CNT network embedded in the microstructured surface (Figure 2e).

The microstructured PDMS film has a similar topography as the screen meshes, as shown in the optical images (Figure 2d, Figure S3, Supporting Information). These mesh-molded microstructures are very uniform, periodic, and highly tunable by using different meshes as molds. Figure 2e gives the cross-sectional image of sliced PDMS/CNT microstructure. It shows that the conductive CNT layer is firmly embedded in rather than attached to the PDMS microstructure surface, which could greatly improve the robustness of the conductive microstructures as verified in Figure S4, Supporting Information. From the surface profile (Figure 2e), regular and periodic micro-patterns with ≈75 and ≈27 μm height are alternately observed, corresponding to alternately woven microfibers of the screen mesh mold. Scanning electron microscopy (SEM) images in Figure 2f, g and Figure S5, Supporting Information, show more clearly the morphology of the PDMS/CNT

microstructures, which are very similar to the topography of screen meshes. In the high-resolution SEM images (Figure S6, Supporting Information), single CNT could also be observed on PDMS/CNT microstructure. This proposed microstructure fabrication strategy achieves a good balance between fabrication cost, scalability, and microstructure quality (i.e., uniformity, regularity, and periodicity). Moreover, this method shows excellent microstructural tunability from tens of micrometers to thousands of micrometers, widely broadening their application range in manufacturing pressure sensors for different purposes.

Moreover, we propose a printable side-by-side electrode configuration for scalable manufacturing of pressure sensors when combined with the mesh-molded pressure-sensing microstructures. Printing techniques show good potential for producing flexible electronics through cost-effective and high-throughput processes. Here, we use inkjet printing to fabricate the side-by-side electrodes on a flexible substrate. Inkjet printing is a non-contact, digital, and additive printing method with minimal waste of materials (Figure 3a). Additionally, the sensor design layout can be easily changed. A small gap of 200 μm is set between the side-by-side electrodes (2 mm × 2 mm) with a trace line of 300 μm. Silver ink is printed on a 125 μm polyethylene naphthalate (PEN) substrate. After drying and sintering, flexible and highly conductive silver electrode patterns can be obtained, as shown in Figure 3b. The

optical microscope images show continuous silver pads with $\approx 197 \mu\text{m}$ gaps and $\approx 312 \mu\text{m}$ trace lines printed on the flexible PEN substrate (Figure 3c,d).

2.3. Sensor Working Mechanism

Most of the reported pressure sensors use top–bottom electrode configurations, as illustrated in Figure 3e,f. The fundamental working mechanism for this class of pressure sensors relies on the change of total resistance of the sensor circuit upon pressure. The change in total resistance is related to a variation of contact resistance (R_{contact}) between the conductive microstructure and the counter electrode. The total resistance is also dependent on the geometry used in order to make the electrical connection between the two electrodes, resulting in an intrinsic resistance ($R_{\text{intrinsic}}$), which is related to the distance (L) between the connection point and the active sensing area, as shown in Figure 3e,f. At low pressure, R_{contact} is very high and dominates for the total resistance, since the contact area between the microstructure and the counter electrode is small. However, at high pressure, R_{contact} decreases dramatically, as the contact area becomes larger, and $R_{\text{intrinsic}}$ of fixed values dominates for the total resistance.

The interlocked geometry used in Figure 3e shows high total resistance, resulting from a large contribution from two $R_{\text{intrinsic}}$ and a variable R_{contact} . Sensors with interlocked microstructures show a sharp change in total resistance at low pressure. This is because both layers of the interlocked conductive microstructures are soft and elastic, and they could come into full contact with each other under small pressure. As pressure increases, a saturation in total resistance is observed, resulting in a relatively narrow range of operation (with 30 kPa), as shown in Figure 3h. This saturation occurs when the microstructures are in full contact and the $R_{\text{intrinsic}}$ of fixed values dominates.

A larger range of operation can be achieved by replacing one conductive microstructure with a flat, highly conductive electrode, as shown in Figure 3f. In this geometry, the total resistance is smaller, with contribution of one $R_{\text{intrinsic}}$ and a variable R_{contact} . As pressure increases, a slow slope in resistance change is observed due to the moderate change in contact area between the conductive microstructure and the flat electrode, as shown in Figure 3h. At higher pressure values, the variation in resistance is dependent on further increase in contact area and dominated by the large $R_{\text{intrinsic}}$.

In our design (Figure 3g), highly conductive in-plane and side-by-side electrodes separated by a $200 \mu\text{m}$ gap is used to minimize $R_{\text{intrinsic}}$. In addition, this device configuration doubles the variable R_{contact} , since the change in contact area will be measured in two electrodes. In other words, the limiting factor of this sensor geometry is R_{contact} as opposed to being limited by $R_{\text{intrinsic}}$ as in the other configurations. As expected and shown in Figure 3h, at low applied pressure, the initial total resistance of the two side-by-side electrodes is higher than one electrode configuration due to the doubled R_{contact} . At high-pressure values, the two side-by-side electrodes show lower total resistance than one electrode configuration due to the minimized $R_{\text{intrinsic}}$ by a small gap resistance (R_{gap}). Thus, this novel

configuration results in a more dramatic resistance variation and a larger operation range when compared with the one electrode configuration and interlocked configuration, respectively.

The sensitivity of the three kinds of pressure sensors compared here is defined as the relative current change in response to applied pressure, that is, $(\Delta I/I_0)/\Delta P$. The pressure sensor with the interlocked conductive microstructures (Figure 3e) shows high sensitivity at low pressure with a narrow working range (limited to $\approx 30 \text{ kPa}$), as indicated in Figure 3i. This kind of pressure sensor is suitable for detecting small pressure (e.g., weak physiological activity, finger touch, etc.) but not capable of detecting relatively large pressure. The one electrode sensor configuration (Figure 3f) results in low sensitivity over a large working range. The two side-by-side electrode configuration (Figure 3g) shows high sensitivity over the entire measured pressure range.

2.4. Electromechanical Response of the Pressure Sensors

The electromechanical characteristics of the pressure sensors are presented in Figure 4. The linear behavior of the I – V curves in Figure 4a indicates that the devices follow Ohm's law and the resistance decreases under pressure. For the other results of Figure 4, a constant voltage of 1 V is applied to the devices. Figure 4b shows the calibration curves of pressure sensors with different mesh microstructures. Pressure sensors with smaller microstructure exhibit relatively higher sensitivity under small pressure, while the signal variation becomes sluggish at higher pressure range. This is because smaller microstructure is easier to deform under pressure, while the deformation get saturated gradually at high pressure, as discussed in Section S1, Supporting Information. In contrast, pressure sensors with larger microstructure exhibit lower sensitivity but broader working range. This is due to that larger microstructure is more resistant to pressure-induced deformation. It is observed that these pressure sensors can detect pressure as high as 1000 kPa. Such a broad working range is rarely achieved for microstructure-based pressure sensors. Moreover, the initial resistance of the sensors could be easily tuned from several kilo-ohms to hundreds of mega-ohms (≈ 5 orders of magnitude) by adjusting the tightness between the top conductive microstructure and the bottom electrodes. Thus, the pressure-sensing behaviors (Figure 4c) and sensor sensitivity (Figure 4d) are also highly tunable by regulating the initial resistance. For some application (e.g., subtle physiological signal detection), high sensitivity is necessary for good signal recognition. In contrast, for certain application (e.g., foot pressure monitoring), low sensitivity but high-pressure detecting capability is needed for stable signal output. Notably, our pressure sensors can meet these requirements readily by tuning the microstructure size as well as the initial resistance to get a desirable sensitivity and working range.

We also evaluate the lowest detection limit of our pressure sensors. As shown in Figure 4e, upon loading a grain of rice (24 mg, corresponding to 7.4 Pa) on a sensor, an obvious increase in current could be observed, indicating a very low detection limit. Additionally, our pressure sensor displays an instantaneous response to both loading and unloading of

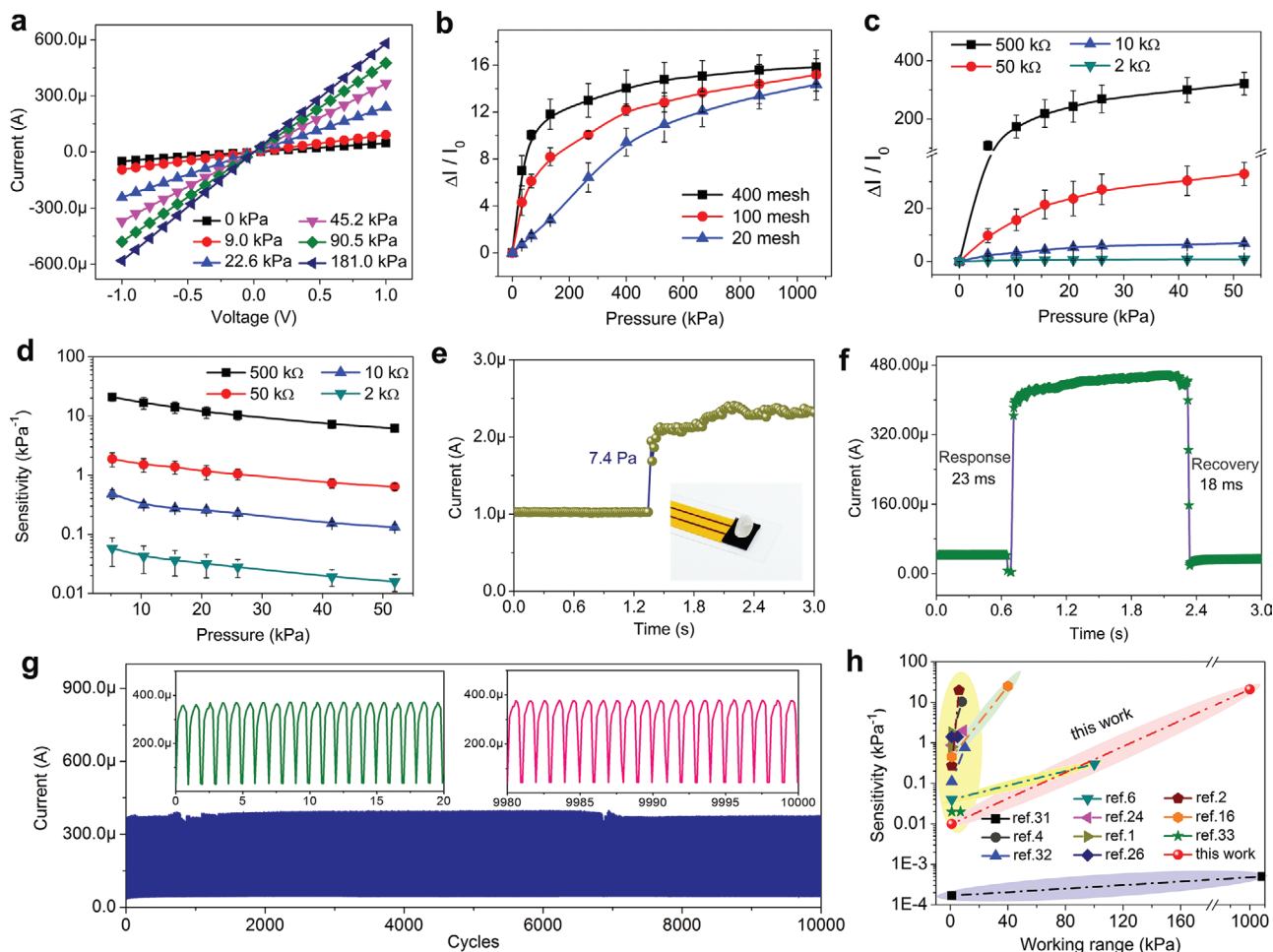


Figure 4. Electromechanical characteristics of the pressure sensors. a) I - V curves of the pressure sensor under different applied pressures. b) Calibration curves of pressure sensors with different microstructure sizes (larger mesh count corresponds to smaller microstructure). c) Calibration curves of pressure sensors with different initial resistances. d) Sensitivity of pressure sensors with different initial resistances. e) Current change with the application of a grain of rice (24 mg, corresponding to 7.4 Pa) on the pressure sensor. f) Response and recovery speed of the pressure sensor. g) Performance of the pressure sensor with cyclic loading–unloading of a high pressure (140 kPa) for 10000 cycles at a frequency of 1 Hz. h) Comparison in sensitivity and working range of our scalable pressure sensors and previously reported devices.^[1,2,4,6,16,24,26,31–33]

external pressure. Pressure sensors with 100 mesh microstructure show a response time of 23 ± 7 ms and a recovery time of 18 ± 4 ms (Figure 4f). Smaller microstructure gives rise to higher response/recovery speed of the sensors, as discussed in Section S2, Supporting Information. Furthermore, the devices also exhibit excellent durability and reliability when repeatedly loading/unloading a high pressure of 140 kPa for 10000 cycles at a frequency of 1 Hz (Figure 4g). Based on the performance mentioned above, we compare our pressure sensors with other recently reported pressure sensors, as presented in Figure 4h and Table S1, Supporting Information. Our pressure sensors show comparable performance in terms of detection limit, response/recovery speed, and reliability, but exhibit much superior performance in working range (up to 1000 kPa), sensitivity (0.01 – 20.9 kPa^{-1}), sensor tunability as well as sensor miniaturization (down to 4 mm \times 2 mm). Together with the superior scalability and cost-efficiency, such pressure sensors are very promising and competitive for practical application.

2.5. Various Human Activities Monitoring and Spatial Pressure Mapping

Due to the low detection limit and broad working range, our flexible pressure sensors are capable of monitoring both small and large human physiological activities. To explore their practical applications, we first attached a pressure sensor to the wrist of a healthy subject (27-year-old male) to record the artery pulse signal. As shown in Figure 5a and Movie S1, Supporting Information, the wrist pulse could be read out accurately from the time-dependent current signals with a periodicity of 73 beats per min. A typical artery pulse waveform consists of three distinguishable peaks, that is, P_1 , P_2 , and P_3 ,^[34,35] as shown clearly in the inset of Figure 5a. Other subtle physiological signals (e.g., pronouncing, coughing, swallowing, etc.) can also be monitored with our pressure sensors (Figure S7, Supporting Information). Besides, our pressure sensors can be used to “feel” human touch. As shown in Figure 5b and Movie S2, Supporting Information, both

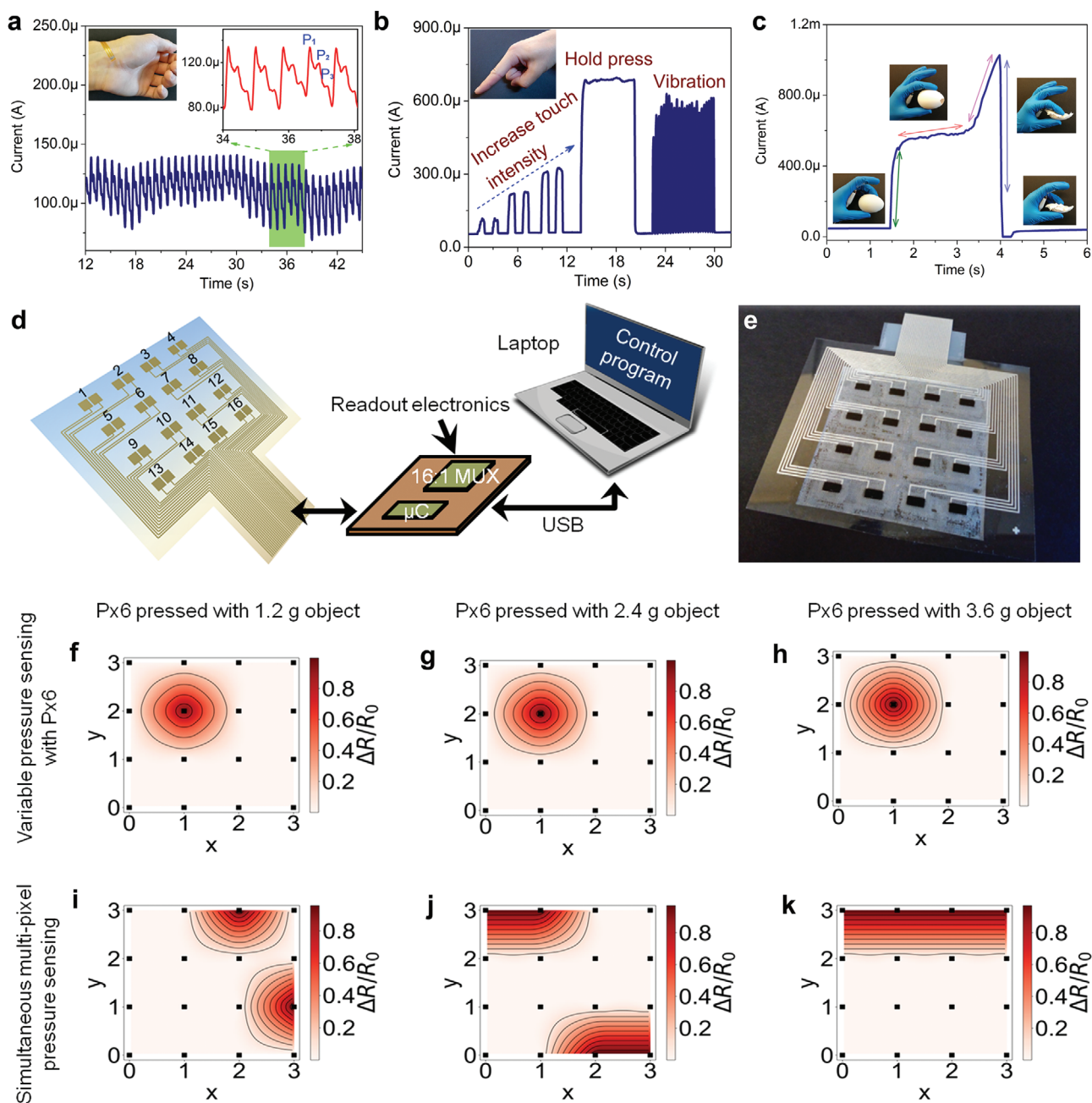


Figure 5. Applications of the pressure sensors for various human physiological activities monitoring and spatial pressure mapping. a) Photograph of a flexible pressure sensor attached on the wrist and the recorded pulse signals as well as an expanded pulse wave. b) The recorded electrical signals when a finger applies static pressure of different values and dynamic pressure vibration on the device. c) Photographs and continuously recorded signal of a pressure sensor mounted on the finger pad during grasping and crushing an egg shell. d) Schematic illustration showing the electrode array with 4×4 pixels for e-skin application and the corresponding pixel numbers. The electrode of the e-skin is connected to a custom-designed readout circuit board for real-time pressure mapping. e) Photograph of the fabricated e-skin. f–h) Spatial mapping of resistance changes when objects with ≈ 1.2 g (f), ≈ 2.4 g (g), and ≈ 3.6 g (h) are placed on pixel 6. i) Corresponding mapping of resistance changes with two batteries (≈ 11.0 g) put on pixels 3 and 12. j, k) Corresponding resistance mapping when two fingers press on pixels 1, 2, 15, 16 (j) and 1, 2, 3, 4 (k), respectively.

static press with different intensity and dynamic vibration could be detected in real-time. Moreover, a pressure sensor was employed to continuously monitor the pressure variation during grasping and crushing an egg shell. Based on the recorded signal (Figure 5c), the whole process could be divided into four stages, including touching, holding, squeezing, and

breaking, respectively. Additionally, we demonstrate the potential applications of the devices for monitoring the pressure of an artificial vessel (Figure S8, Supporting Information) and joint bending motions (Figure S9, Supporting Information). These results provide the evidence that our flexible and wearable pressure sensors are adequate for dynamic interaction

between a machine and human and could be promising for manufacturing wearable diagnostic devices, service robots, artificial limbs, and other smart systems.

Moreover, we fabricate a pressure sensitive e-skin with 4×4 pixels via the combination of printed silver electrodes and patterned conductive microstructure. A piece of e-skin (Figure 5e) could be easily assembled by attaching the patterned conductive microstructure onto the printed electrodes (Figure S10, Supporting Information). To realize spatial pressure mapping in real-time, the e-skin is connected to a custom data acquisition circuit board with 16 measurement channels (as illustrated in Figure 5d), which can communicate with a computer. A continuous mapping of the resistance change can be reconstructed on the computer, as shown in Movie S3, Supporting Information. We first verify the functionality of every pixel in this e-skin (Figure S11, Supporting Information). Then, we apply different pressure on a randomly selected pixel (pixel 6 as an example) by placing objects with ≈ 1.2 g, ≈ 2.4 g, and ≈ 3.6 g, respectively. As shown in the reconstructed color mapping (Figure 5f–h), the e-skin can distinguish the difference in magnitude of the applied pressure. The capability of our e-skin to resolve spatial pressure distribution is also evaluated by placing two batteries on pixels 3 and 12. The spatial resistance variation is consistent with the battery location, as shown in Figure 5i. Next, two fingers were pressed on region A (with pixels of 1, 2, 15, and 16) and region B (with pixels of 1, 2, 3, and 4), respectively. The reconstructed color mappings are also in good correlation with the pressure distribution (Figure 5j,k). These results demonstrate the good capability of our e-skin to resolve spatial distribution as well as the magnitude of the applied pressure.

2.6. Smart Insole for Simultaneous Mapping of Foot Pressure and Temperature

Our feet provide the primary interactive surface with the environment during locomotion. Hence, foot health is of great significance to our well-being. Recently, smart insoles for foot pressure detection have been reported,^[3,16,36,37] which provide feasible solutions for footwear design, sports performance analysis, and injury prevention. Except for foot pressure, foot temperature is also crucial to our health, as foot temperature is a good indicator for our blood circulation condition and can also affect the blood circulation process in our body. Additionally, for diabetes patients who are at risk of developing a foot ulcer, there is an increase in foot temperature before the foot ulcer develops due to inflammation and enzymatic autolysis of the tissue.^[38] Therefore, monitoring of foot temperature is of great importance for early disease recognition and foot ulcer prevention. Based on these aspects, integration of foot temperature monitoring and foot pressure mapping into a single smart insole through compatible manufacturing process could greatly extend the insole's functions and versatility, which, however, has not been reported in the literature.

Here, we design and fabricate a flexible smart insole for both foot pressure and temperature monitoring simultaneously via a scalable and low-cost fabrication process. **Figure 6a** shows the fabricated smart insole, which consists of 12 pressure sensors

and four printed thermistors (i.e., temperature sensors). As illustrated in Figure 6b, the 12 pressure sensors are placed at anterior, medial, lateral, and posterior regions, respectively, according to gait kinetics as well as normal and pathological foot anatomy.^[39] The four thermistors are distributed at medial, lateral, and posterior regions thus to monitor the temperature at different foot positions. The whole smart insole is fabricated through three steps: 1) inkjet printing electrode patterns on the flexible substrate, 2) stencil printing the thermistors, and 3) installing the pressure-sensing layers and encapsulating the insole with a Kapton tape film. The resultant smart insole can be connected to a custom data acquisition circuit board as mentioned above to record pressure as well as temperature signals in real time. The calibration process for the pressure sensors and thermistors is described in Figures S12 and S13, Supporting Information.

As shown in Figure 6c, when a person steps on the smart insole, the measured temperature rises from 24.5 °C in the beginning and gradually increases to ≈ 29.9 °C, which is the normal skin temperature of the foot.^[40] With the foot taken off from the insole, the temperature goes back to the original value slowly. On the other hand, as shown in Figure 6d, the signals of the 12 pressure sensors exhibit prompt increase and decrease when the foot is placed on and taken off from the insole, respectively, and keep relatively stable when the foot is stepped on the insole. Foot pressure mapping and temperature distribution can be reconstructed from the acquired signals, as shown in Figure 6e. It is noticed that the highest pressure is detected at the posterior region. Medium pressure is distributed at the anterior and medial parts, and low pressure is applied on the lateral area. Such foot pressure distribution is in good consistency with the results reported in the literature.^[3,39] Moreover, during the dynamic walking process, signals variation of the 12 pressure sensors could also be recorded continuously, as given in Figure 6f. Based on these continuous signals, the evolution of foot pressure mapping can be reconstructed as shown in Figure 6g. Such foot pressure evolution can provide abundant information for footwear design, sports performance analysis, as well as gait and posture research.

In addition, we also evaluate the capability of our smart insole in monitoring foot pressure and temperature under different temperature settings. As shown in Figure S14a, Supporting Information and Figure 6h, when a cold foot (the foot was immersed into cold water of 15 °C for a while and quickly dried with a towel) is first stepped on the insole for a while and then taken off, the recorded foot temperature shows rapid drop from 24.5 °C to ≈ 19.5 °C and then recovers slowly. In contrast, when a hot foot (the foot was immersed into hot water of 45 °C for a while and quickly dried with a towel) steps on the insole for a while (Figure S14b, Supporting Information and Figure 6i), the measured average foot temperature exhibits a rise from 24.5 °C to ≈ 32.8 °C, which is higher than normal foot skin temperature. These results verify that our smart insole is capable of monitoring foot temperature continuously. Notably, the foot pressure distributions detected under different foot temperatures (Figure 6e for normal foot, Figure 6h for a cold foot, and Figure 6i for a hot foot) are similar to each other, demonstrating that temperature change

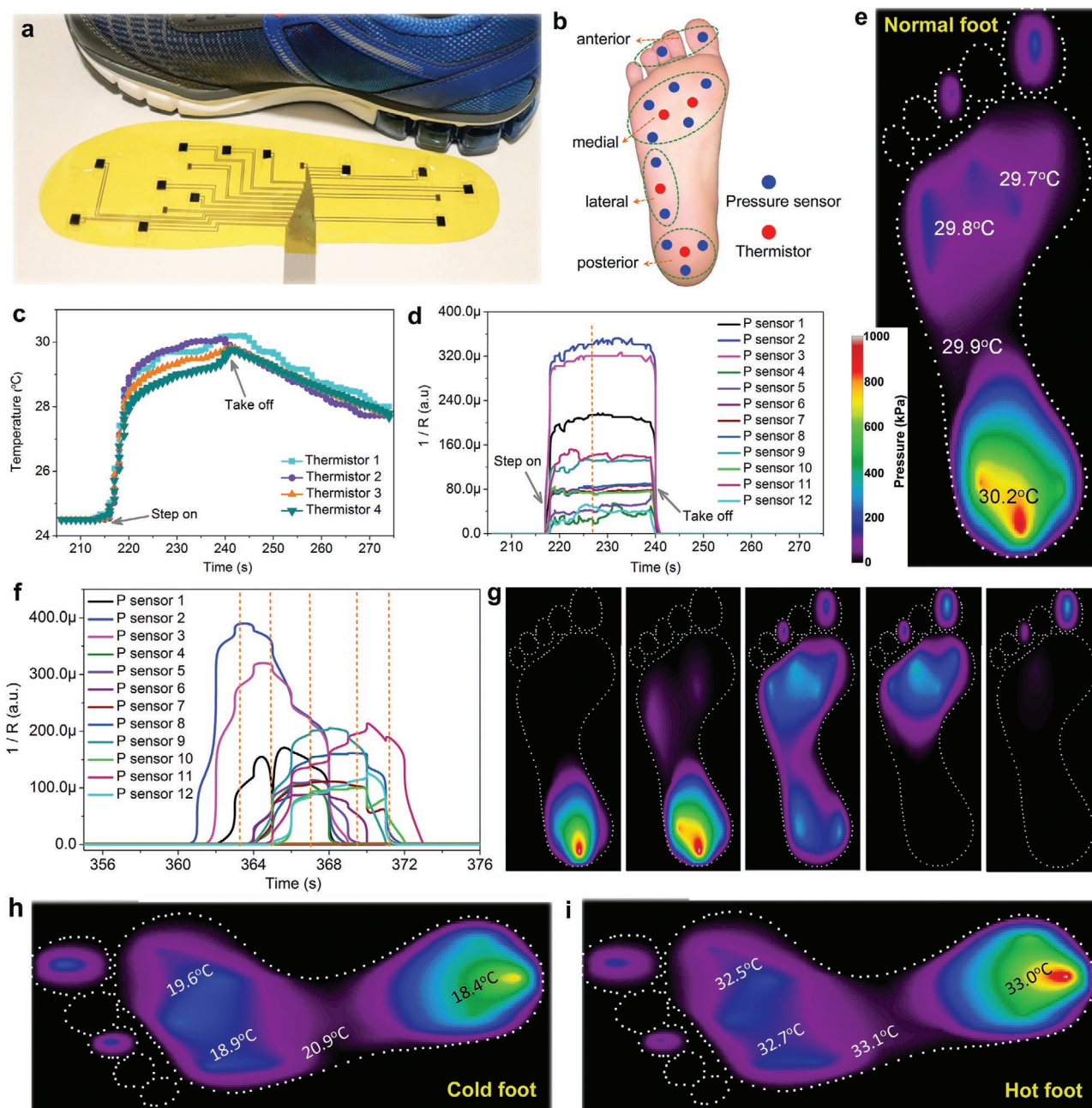


Figure 6. Flexible smart insole for foot pressure and temperature monitoring. a) Photograph of the fabricated flexible smart insole. b) Schematic showing the corresponding positions of the 12 pressure sensors and the four printed thermistors on the foot. c,d) The recorded response curves of the four thermistors and the 12 pressure sensors (P sensor) when a normal foot is stepped on and then taken off from the smart insole. e) The reconstructed foot pressure and temperature distribution of the foot. The scale bar applies to all the pressure mappings in this figure. f) Continuously recorded signal variations of the 12 pressure sensors with a foot walking on the smart insole. g) Evolution of the extracted foot pressure mapping during the walking process. h) The reconstructed foot pressure mapping and temperature distribution of a cold foot. i) The reconstructed foot pressure mapping and temperature distribution of a hot foot.

does not impact the pressure mapping capability of the smart insole. All the performance presented above, together with its light weight, good scalability, and cost-efficiency, makes the smart insole appealing for manufacturing wearable healthcare devices, medical diagnostic systems, and smart sports products.

3. Conclusion

In summary, we demonstrated a large-area compliant and cost-effective strategy to fabricate wearable pressure sensors via the combination of mesh-molded microstructures and printed side-by-side electrodes. The proposed mesh-molding technique for

pressure-sensing microstructure fabrication enables achievement of a good balance among fabrication cost, scalability, and microstructure quality (uniformity, periodicity, and tunability). The printed electrodes with side-by-side configuration endow our pressure sensors with high sensitivity and broad working range. When compared with the reported flexible pressure sensors, our devices show comparable performance such as low operating voltage (1 V), high sensitivity (20.9 kPa⁻¹), low detection limit (7.4 Pa), fast response/recovery time (23/18 ms), excellent reliability (10 000 cycles), but much better performance in terms of working range (up to 1000 kPa), sensor tunability, sensor size (down to 4 mm × 2 mm) and capability to form self-defined sensor arrays. More importantly, our sensors exhibit superior scalability and cost efficiency. We demonstrated the potential applications of our pressure sensors in monitoring various human physiological activities and resolving spatial distribution and magnitude of applied pressure as an e-skin. Furthermore, we developed a smart insole for both foot pressure and temperature monitoring based on printing techniques, which can greatly extend its application range compared to conventional smart insoles with only pressure-sensing function. Considering the overall high-performance, good scalability, and impressive versatility, the technique and demonstrations presented in this work can be applied toward affordable and accessible personal electronics and biomedical devices in the near future.

4. Experimental Section

Scalable Fabrication of PDMS/CNT Conductive Microstructure via Mesh-Molding Strategy: Stainless-steel screen meshes with different mesh counts (provided by TWP Inc.) were used to fabricate uniform, periodic, and size-tunable conductive microstructures. First, a pre-cleaned screen mesh was cut into the desired size and heated on a hotplate with the temperature set to 190 °C. Then, a piece of polystyrene (PS) sheet (1 mm in thickness) was placed on the heated screen mesh for 5 min to soften the PS sheet, followed by pressing the softened PS sheet with 300 kPa to transfer the mesh structure to the PS sheet. After cooling down, the screen mesh was peeled off from the PS sheet, and PS sheet with inverse mesh structure was obtained. Then, the microstructured PS sheet was used as a template, onto which a layer of multiwalled CNT (US Research Nanomaterials, Inc., >95%, OD: 10–20 nm) was spray-coated using CNT suspension (1 mg mL⁻¹, dispersed in ethyl alcohol) with an airbrush under 2.5 bars air pressure. Subsequently, PDMS precursor mixture (Dow Corning Sylgard 184; the weight ratio of base to cross-linker varies from 5:1 to 10:1) was stirred, degassed, and then cast onto the PS mold with conductive CNT layer. Finally, the PDMS was cured at 60 °C for 2 h and carefully peeled off from the micro-patterned PS mold, resulting in a uniform and periodic conductive PDMS/CNT microstructure with robust CNT layer embedded in the microstructure surface. For pressure sensor array (Figure 5e) fabrication, a laser-cut Kapton tape mask (60 μm in thickness) was attached on the micro-patterned PS mold before spray-coating CNT, thus to create conductive CNT patterns in the eventual PDMS/CNT conductive film.

Electrode Pattern Printing: 125 μm thick polyethylene naphthalate (PEN) film (Q65HA, Teijin-DuPont) was used as the substrate for inkjet printing the electrode patterns. Silver ink (Silverjet DGP 40LT-15C, Advanced Nano Products Co., Ltd.) was printed using a Dimatix inkjet printer (DMP-2800) with 25 μm drop spacing. Subsequently, the printed electrodes were sintered (150 °C for 30 min) to create conductive patterns. For pressure sensors array preparation, a patterned electrode array with 4 × 4 pixels was screen-printed on PET substrate (125 μm) using silver ink (126-33, Creative Materials, Inc.). The printed electrodes were annealed at 100 °C for 10 min.

Pressure Sensor Assembly: Pressure sensors were constructed by assembling the scalable conductive PDMS/CNT microstructure and the printed electrodes with side-by-side configuration. Specifically, microstructured PDMS/CNT conductive film was cut into small pieces with the desired size, and then fixed on top of the side-by-side electrodes using Kapton tape. The initial resistance of the sensors could be easily tuned from several kilo-ohms to hundreds of mega-ohms by adjusting the degree of tightness between the top conductive PDMS/CNT microstructure and the bottom electrodes. Fabrication of pressure sensors of different electrode configurations is illustrated in Section S3, Supporting Information.

Smart Insole Construction: To fabricate the smart insole for both foot pressure and temperature monitoring, 12 pressure sensors and four thermistors were employed. The electrode patterns were inkjet-printed using the conditions mentioned above. The small gap of the side-by-side electrodes was set to 200 μm for pressure sensors and 140 μm for thermistors. Then, four thermistors were stencil printed on top of the corresponding electrodes using a 60 μm thick laser-cut Kapton tape mask and a glass slide. The thermistors were comprised of 6:2:1 weight ratio of NiO nanopowder (<50 nm, Sigma-Aldrich), SSB binder (Targray Technology), and deionized (DI) water. The printed thermistors were then sintered for 2 h at 140 °C. After that, 12 pressure sensors were constructed by placing 12 pieces of microstructured PDMS/CNT conductive films (4 mm × 6 mm, with 5:1 base to cross-linker ratio) of the residual pixels of the printed electrodes. Finally, the thermistors and pressure sensors were encapsulated by attaching a layer of 60 μm thick Kapton tape on the top of the whole insole to avoid electrode scratching and the effect of moisture on the thermistors.

Characterization and Measurement: Electrical resistance measurements were performed using a Keithley 2400 Source Meter. The electrical signal of the sensors was collected on a Keithley 2601A Source Meter and Agilent Semiconductor Device Analyzer (B1500A). The optical observation was conducted on an optical microscope (Eclipse 50i, Nikon). A Dektak profiler (Veeco 6M) was used for profile measurement. SEM observation was carried out on a Zeiss microscope with EHT value of 5 kV. Pressure measurement was conducted on a custom setup based on a computer-controlled movable stage and a force gauge (M5, Mark-10). Pressure calculation is illustrated in Section S4, Supporting Information. Human physiological activities monitoring experiments performed on human subjects were carried out with informed consent under the approval of the University of California, Berkeley Institutional Review Board, protocol ID number 2018-11-11567.

Supporting Information

Supporting Information is available from the Wiley Online Library or from the author.

Acknowledgements

X.W. and Y.K. contributed equally to this work. This work was supported in part by the Bakar Fellows Program, the National Science Foundation under Grant No. 1610899, and FlexTech Alliance under Grant No. AFOSR 42299. X.W. acknowledges the support from China Scholarship Council under Grant No. 201706240083. J.Z. acknowledges the support from International Partnership Program of Chinese Academy of Sciences (Grant No. 112111KYSB20160061) and NSFC (Grant No. 61888102).

Conflict of Interest

X.W., Y.K., J.T., and A.C.A. are inventors on a pending patent application (Provisional No. 62/835129) filed through the University of California, Berkeley. The other authors declare no conflict of interest.

Keywords

electronic skin, periodic microstructures, pressure sensors, side-by-side electrodes

Received: November 22, 2019
Published online: January 15, 2020

- [1] X. Wang, Y. Gu, Z. Xiong, Z. Cui, T. Zhang, *Adv. Mater.* **2014**, *26*, 1336.
- [2] M. Jian, K. Xia, Q. Wang, Z. Yin, H. Wang, C. Wang, H. Xie, M. Zhang, Y. Zhang, *Adv. Funct. Mater.* **2017**, *27*, 1606066.
- [3] Y. Lee, J. Park, S. Cho, Y.-E. Shin, H. Lee, J. Kim, J. Myoung, S. Cho, S. Kang, C. Baig, H. Ko, *ACS Nano* **2018**, *12*, 4045.
- [4] C.-L. Choong, M.-B. Shim, B.-S. Lee, S. Jeon, D.-S. Ko, T.-H. Kang, J. Bae, S. H. Lee, K.-E. Byun, J. Im, Y. J. Jeong, C. E. Park, J.-J. Park, U.-I. Chung, *Adv. Mater.* **2014**, *26*, 3451.
- [5] B. C.-K. Tee, A. Chortos, R. R. Dunn, G. Schwartz, E. Eason, Z. Bao, *Adv. Funct. Mater.* **2014**, *24*, 5427.
- [6] C. M. Boutry, Y. Kaizawa, B. C. Schroeder, A. Chortos, A. Legrand, Z. Wang, J. Chang, P. Fox, Z. Bao, *Nat. Electron.* **2018**, *1*, 314.
- [7] Z. Wang, S. Guo, H. Li, B. Wang, Y. Sun, Z. Xu, X. Chen, K. Wu, X. Zhang, F. Xing, L. Li, W. Hu, *Adv. Mater.* **2019**, *31*, 1805630.
- [8] J. Park, M. Kim, Y. Lee, H. S. Lee, H. Ko, *Sci. Adv.* **2015**, *1*, e1500661.
- [9] J. Park, Y. Lee, J. Hong, Y. Lee, M. Ha, Y. Jung, H. Lim, S. Y. Kim, H. Ko, *ACS Nano* **2014**, *8*, 12020.
- [10] L. Pan, A. Chortos, G. Yu, Y. Wang, S. Isaacson, R. Allen, Y. Shi, R. Dauskardt, Z. Bao, *Nat. Commun.* **2014**, *5*, 3002.
- [11] Y. S. Zhou, G. Zhu, S. Niu, Y. Liu, P. Bai, Q. Jing, Z. L. Wang, *Adv. Mater.* **2014**, *26*, 1719.
- [12] C. Pang, G.-Y. Lee, T. Kim, S. M. Kim, H. N. Kim, S.-H. Ahn, K.-Y. Suh, *Nat. Mater.* **2012**, *11*, 795.
- [13] F.-R. Fan, L. Lin, G. Zhu, W. Wu, R. Zhang, Z. L. Wang, *Nano Lett.* **2012**, *12*, 3109.
- [14] J.-G. Sun, T. N. Yang, I.-S. Kuo, J.-M. Wu, C.-Y. Wang, L.-J. Chen, *Nano Energy* **2017**, *32*, 180.
- [15] Z. Qiu, Y. Wan, W. Zhou, J. Yang, J. Yang, J. Huang, J. Zhang, Q. Liu, S. Huang, N. Bai, Z. Wu, W. Hong, H. Wang, C. F. Guo, *Adv. Funct. Mater.* **2018**, *28*, 1802343.
- [16] Y. Pang, K. Zhang, Z. Yang, S. Jiang, Z. Ju, Y. Li, X. Wang, D. Wang, M. Jian, Y. Zhang, R. Liang, H. Tian, Y. Yang, T.-L. Ren, *ACS Nano* **2018**, *12*, 2346.
- [17] Q.-J. Sun, X.-H. Zhao, Y. Zhou, C.-C. Yeung, W. Wu, S. Venkatesh, Z.-X. Xu, J. J. Wylie, W.-J. Li, V. A. L. Roy, *Adv. Funct. Mater.* **2019**, *29*, 1808829.
- [18] C. M. Boutry, M. Negre, M. Jorda, O. Vardoulis, A. Chortos, O. Khatib, Z. Bao, *Sci. Rob.* **2018**, *3*, eaau6914.
- [19] C.-B. Huang, S. Witomska, A. Aliprandi, M.-A. Stoeckel, M. Bonini, A. Ciesielski, P. Samori, *Adv. Mater.* **2019**, *31*, 1804600.
- [20] S. Lee, A. Reuveny, J. Reeder, S. Lee, H. Jin, Q. Liu, T. Yokota, T. Sekitani, T. Isoyama, Y. Abe, Z. Suo, T. Someya, *Nat. Nanotechnol.* **2016**, *11*, 472.
- [21] H.-B. Yao, J. Ge, C.-F. Wang, X. Wang, W. Hu, Z.-J. Zheng, Y. Ni, S.-H. Yu, *Adv. Mater.* **2013**, *25*, 6692.
- [22] R. Li, Y. Si, Z. Zhu, Y. Guo, Y. Zhang, N. Pan, G. Sun, T. Pan, *Adv. Mater.* **2017**, *29*, 1700253.
- [23] X. Wu, Y. Han, X. Zhang, Z. Zhou, C. Lu, *Adv. Funct. Mater.* **2016**, *26*, 6246.
- [24] H. Park, Y. R. Jeong, J. Yun, S. Y. Hong, S. Jin, S.-J. Lee, G. Zi, J. S. Ha, *ACS Nano* **2015**, *9*, 9974.
- [25] B. Zhu, Z. Niu, H. Wang, W. R. Leow, H. Wang, Y. Li, L. Zheng, J. Wei, F. Huo, X. Chen, *Small* **2014**, *10*, 3625.
- [26] S. Gong, W. Schwalb, Y. Wang, Y. Chen, Y. Tang, J. Si, B. Shirinzadeh, W. Cheng, *Nat. Commun.* **2014**, *5*, 3132.
- [27] Y. Ma, N. Liu, L. Li, X. Hu, Z. Zou, J. Wang, S. Luo, Y. Gao, *Nat. Commun.* **2017**, *8*, 1207.
- [28] N. Luo, Y. Huang, J. Liu, S.-C. Chen, C. P. Wong, N. Zhao, *Adv. Mater.* **2017**, *29*, 1702675.
- [29] G. Y. Bae, S. W. Pak, D. Kim, G. Lee, D. H. Kim, Y. Chung, K. Cho, *Adv. Mater.* **2016**, *28*, 5300.
- [30] N. Luo, W. Dai, C. Li, Z. Zhou, L. Lu, C. C. Y. Poon, S.-C. Chen, Y. Zhang, N. Zhao, *Adv. Funct. Mater.* **2016**, *26*, 1178.
- [31] S.-J. Woo, J.-H. Kong, D.-G. Kim, J.-M. Kim, *J. Mater. Chem. C* **2014**, *2*, 4415.
- [32] C. M. Boutry, A. Nguyen, Q. O. Lawal, A. Chortos, S. Rondeau-Gagné, Z. Bao, *Adv. Mater.* **2015**, *27*, 6954.
- [33] G. Ge, Y. Zhang, J. Shao, W. Wang, W. Si, W. Huang, X. Dong, *Adv. Funct. Mater.* **2018**, *28*, 1802576.
- [34] Y. Chu, J. Zhong, H. Liu, Y. Ma, N. Liu, Y. Song, J. Liang, Z. Shao, Y. Sun, Y. Dong, X. Wang, L. Lin, *Adv. Funct. Mater.* **2018**, *28*, 1803413.
- [35] X. Fan, Y. Huang, X. Ding, N. Luo, C. Li, N. Zhao, S.-C. Chen, *Adv. Funct. Mater.* **2018**, *28*, 1805045.
- [36] C. Deng, W. Tang, L. Liu, B. Chen, M. Li, Z. L. Wang, *Adv. Funct. Mater.* **2018**, *28*, 1801606.
- [37] S. Chen, B. Zhuo, X. Guo, *ACS Appl. Mater. Interfaces* **2016**, *8*, 20364.
- [38] S. A. Bus, *Diabetes/Metab. Res. Rev.* **2016**, *32*, 221.
- [39] J. T.-M. Cheung, M. Zhang, *Arch. Phys. Med. Rehabil.* **2005**, *86*, 353.
- [40] N. Papanas, K. Papatheodorou, D. Papazoglou, S. Kotsiou, E. Maltezos, *J. Diabetes Sci. Technol.* **2010**, *4*, 803.